Available online at www.sciencedirect.com
SCIENCE DIRECT®
ELSEVIER
Ultramicroscopy 96 (2003) 385–400
ultramicroscopy
www.elsevier.com/locate/ultramic

Improving energy resolution of EELS spectra: an alternative to the monochromator solution

A. Gloter*, A. Douiri, M. Tencé, C. Colliex

Laboratoire de Physique des Solides, Université Paris-Sud, UMR 8502, Orsay 91405, France

Received 17 June 2002; accepted 27 October 2002

Abstract

In this paper, we propose a numerical method which can routinely improve the energy resolution down to 0.2–0.3 eV of electron energy-loss spectra acquired in a transmission electron microscope. The method involves measurement of the point-spread function (PSF) corresponding to the spectrometer aberration and to the incident energy spread, and then an inversion of this PSF so as to restore the spectrum. The chosen algorithm is based on an iterative calculation of the maximum likelihood solution known to be very robust against small errors in the PSF used. Restorations have been performed on diamond and graphite C-K edges acquired with an initial energy resolution of around 1 eV. After reconstruction, the sharp core exciton lines become clearly visible for both compounds and the final energy resolution is estimated to be about 200–300 meV. In the case of graphite, restorations involving both energy resolution and angular resolution have been successfully conducted. Finally, restorations of Fe $L_{2,3}$ and O-K edges measured for various iron oxides will be shown.

PACS: 78.90.+t; 61.16.Bg; 78.70.En

Keywords: EELS; Deconvolution; Energy resolution

1. Introduction

Improving routinely the energy resolution of transmission electron microscopy (TEM) acquired electron energy-loss spectra (EELS) down to 0.2–0.3 eV is a very important challenge, which has focussed the efforts of many researchers. Implementation of energy monochromators has been demonstrated to provide an improvement down to 0.1–0.2 eV at the cost of noticeable loss of intensity [1–5]. Numerical restoration by the zero loss (ZL) peak using a maximum entropy method, has also been investigated [6]. In the present study, we demonstrate the efficiency of the Richardson–Lucy (RL) algorithm [7,8] for improving energy resolution of EELS acquired with a CCD detector. The RL algorithm has already been extensively tested and successfully applied to image restoration in other scientific fields (in particular, the image restoration of Hubble space telescope). Up to now, the only report of the use of RL method in the field of TEM microscopy seems to be due to

*Corresponding author. Tel.: +33-0169155371; fax: +33-0169158004.
E-mail address: gloter@lps.u-psud.fr (A. Gloter).

0304-3991/03/$ - see front matter
doi:10.1016/S0304-3991(03)00103-7

Zhuo [9], who applied the RL procedure to correct the CCD point-spread function (PSF) for high-resolution images, electron diffraction patterns and EELS. In the present study, the RL method is specifically applied to the case of EELS with the goal of noticeably improving the energy resolution. The technique includes the simultaneous correction of the CCD PSF, spectrometer aberration figure and energy spread of the electron source. Shown in Fig. 1 is a schematic description of the CCD detector, where some of these spectrometer aberration figures are reproduced. The RL algorithm has been tested for operation either in a 1D domain (the dispersive axis corresponding to the energy loss E) or in a 2D domain (the E-axis and the non-dispersive y-axis). In the later case, spectrum restoration implies the restoration of a 1024×100-pixel image, which requires the use of an image restoration algorithm.

The paper is organized as follows. The RL basic principles are outlined in Section 2, in which we also describe and validate our approach by testing RL for the restoration of a noisy simulated Fe 2p spectrum. In Section 3.1, the method is applied to the diamond C-K edges measured on a synthetic reference compound. Particular attention is devoted to the sharp excitonic feature at this edge. The performance of the RL method is evaluated, when used in a 1D domain (E) or in a 2D domain (E, y). The 2D reconstructions constitute a platform to comment on the suitability of the measured PSF. In Sections 3.2 and 3.3, the 2D restorations obtained for a graphite sample using either a high-convergence probe (HCP, where the convergence angle 2α is around 30 mrad) or a low-convergence probe (LCP, where α is around 1 mrad) are compared. In Section 4, the results of the restoration for the Fe $L_{2,3}$ and the O-K edges from reference mineralogical samples, are shown and discussed. Throughout the paper, the restored spectra are compared to existing published data (X-ray absorption spectroscopy—XAS or EELS), which have not been reproduced but can easily be found in wide-circulation journals or in spectral libraries (See for instance Ref. [10]). The RL method has been tested for a quite large number of edges and conditions in order to check the stability of the algorithm. It is very important to insure that the solution obtained using the RL algorithm can be regarded with confidence.

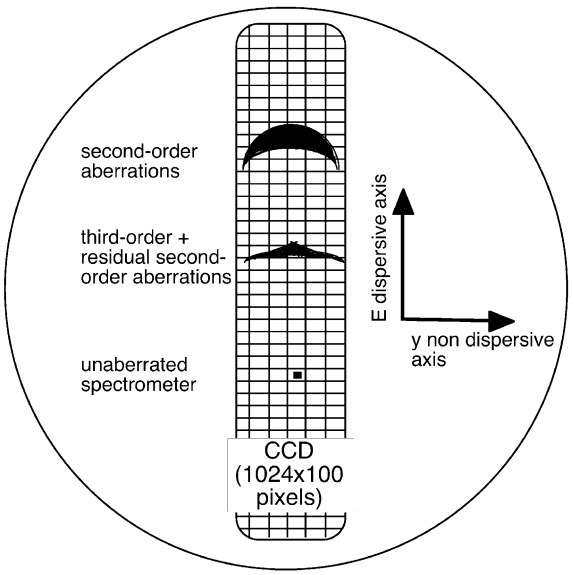

Fig. 1. Schematic view of the CCD detector, with representative aberration figures occurring from a perfectly double focussing spectrometer and two different aberrated spectrometers. For the aberrated spectrometers, the signal coming from the point source gets scattered into an expanded area on the detector, resulting in a degradation of the energy resolution.

2. The Richardson–Lucy algorithm

2.1. Inverse problem

Several numerical methods [11–15] have been recently proposed, to compensate for the optical defect of astrophysical instruments (and, in particular, for Hubble space telescope). The common goal of these methods is to invert the large point spreading caused by the optical system (spherical aberration of the primary mirror) so as to restore the image to the original resolution. We have adopted a similar approach to improve the energy resolution of EELS. In this case, the PSF arises from the optical aberration of the spectrometer, the primary energy spread of the electron beam and the CCD PSF. Of practical importance is the use of a CCD detector to collect the EELS

spectrum (in fact an EELS image) composed of 1024 pixels along the energy dispersive axis and 100 pixels along the non-dispersive axis. The EELS restoration procedure corresponds then to an image restoration procedure.

The most widely used image restoration procedure for astronomical data is the RL algorithm [7,8], which we adapt to EELS image restoration. The conventional RL algorithm can be described in the following way.

The imaging equation states how the true image, which could be the image of a nebula or a 2D image of a C-K edge on the CCD detector of an EELS, is blurred by the PSF:

$$I(i) = \sum_j P(i/j) O_{(j)},$$

where $O_{(j)}$ is the original unblurred object, $P(i/j)$ is the PSF, describing how the signal coming from the true location j gets scattered into the observed pixel i, and $I(i)$ is the noiseless blurred image. If we assume that the effect of defocus for the different energy losses is insignificant, then the PSF does not vary with the position in the EELS detector. This means that $P(i/j) = P(i-j)$ and then, the sum becomes a convolution. If we assume a Poisson distribution for the additive noise, the probability of getting N counts in a pixel when the mean expected number is N_m is given by

$$P(N/N_m) = \frac{e^{-N_m} N_m^N}{N!}.$$

Then, one could define the joint likelihood L of getting the observed $D(i)$ in each pixel given the expected count $I(i)$ by

$$\ln L = \sum_i [D(i)\ln(I(i)) - I(i) - \ln(D(i)!)].$$

The RL deconvolution consists in calculating the maximum likelihood solution in the following iterative form [13]:

$$O_{(j)}^{k+1} = O_{(j)}^k \left(\sum_i \frac{P(i/j) D(i)}{\sum_l P(i/l) O_{(l)}^k} \right) \Bigg/ \left(\sum_i P(i/j) \right), \quad (1)$$

where k is the iterative number and $O_{(j)}^k$ the estimation of the unblurred object at the iteration number k. In this form, the RL algorithm has several advantages:

- As proven by Shepp and Vardi [16], the iterative form converges to the maximum likelihood solution for Poisson statistics in the data. For EELS experiments achieved with a Gatan electron energy filter and a CCD camera, the noise has several origins. In addition to the noise in the original data, the electron–photon–electron conversion, the dark current image and the CCD readout process may introduce noise. The first three types of noise are Poisson-like and the readout noise is Gaussian distributed. In a first approximation, this small Gaussian contribution to the noise has been neglected but a general solution of the RL algorithms including both types of noise have been proposed [13]. Our EELS images have also been corrected for pixel gain variations by collecting an image prior to the experiment using a flat illumination.
- If the observed image is non-negative, the RL algorithm forces the restored image to be non-negative and conserves flux both globally and locally at each iteration. Indeed, it will be shown that the spectrum intensity is well preserved even for data with large dynamic range, such as 2D image of a core-loss spectrum, for which central lines of the detector contain bright features and external lines contain features of weak intensity.
- The restored images are robust against small errors in the PSF. This behavior is important since we estimate the PSF by measuring a ZL spectrum in the vacuum. Incomplete knowledge of the PSF may come from (i) changes in the angular distribution between the ZL and core-loss measurements due to higher angular distributions for inelastic scattering or to diffraction effects, (ii) energy instabilities of the spectrometer and accelerating voltage, and (iii) the non-negligible spectrometer defocus at high energy loss.

Despite its advantages, the RL method has also some inconveniences. In fact, for noisy data, the maximum likelihood approach may not give the most visually pleasing solution. The process of

fitting the data gives rise to strong noise amplification, producing a so-called speckling appearance. This tends to be particularly visible for extended fine structure, which develops fluctuations not representative of any real structure in the spectrum. This is the result of fitting too closely the noise in the image. To reproduce a small noise bump, the image should have a large noise spike and the pixel close to that strong spike should have lower counts to conserve the local flux. This leads to the creation of false objects and wavy structures.

One practical way to limit the noise amplification is to stop the iteration before getting too close to the exact solution of the likelihood maximum. It can simply be achieved by stopping the iteration when the restored image appears too noisy. One may also evaluate the signal-to-noise ratio (S/N) of the image, or just from an area where the true image is known, such as the slowly decreasing pre-edge background in the EELS spectrum, and then stop the iteration for a particular S/N value. Automatic criteria for setting the stopping threshold have also been suggested [17], but they have not been used here since we are interested in monitoring how the spectra vary as the number of iterations is increased.

It has been demonstrated previously that a rudimentary Gaussian pre-filtering of the PSF and the image can improve the S/N ratio of the reconstructed image [18], and we have tested this approach here. Damped versions of RL algorithm have also been demonstrated to limit the noise amplification [19]. Unfortunately, our results using this damped version have only shown a slight improvement in S/N at the cost of some artifacts including instabilities in the convergence and changes in the pre-edge background slope. Thus, the application of damped RL version has not been considered in the present study.

To complete this brief presentation of the used RL algorithm, the raw image, i.e., the as-measured 2D image, has been used as the first iteration step $O_{(j)}^{k=0}$ [13]. Readers interested in more detailed description of RL algorithm may refer to [13,12,20].

2.2. Restoration of a simulated Fe $L_{2,3}$ edge

To check the validity of our Fourier transform-based iterative computation of the RL algorithm, it has first been tested on an image representative of an EELS experiment, using Eq. (1). First of all, one has to define what is the ideal image of a 2D CCD-based EELS experiment. A perfect spectrum could be defined as one that is obtained with the following ideal EELS system. First, the EELS spectrometer is a non-aberrated double-focussing spectrometer with negligible CCD PSF. For a given energy loss, the spectrometer should focus the beam into a single CCD pixel, see Fig. 1. The energy spread ΔE_0 of the incident electron beam should also be negligible compared with the energy dispersion of the spectrometer. A spectrum, characteristic of this system, is presented in Fig. 2(b) and appears as a one-pixel wide spectrum located along the center line of the CCD detector. In this example, the EELS spectrum is a Fe $L_{2,3}$ edge calculated theoretically using an atomic multiplet calculation for an Fe^{3+} ion [21]. The following parameters have been used for the calculation: an octahedral crystal field of strength $10\,Dq = 1.5\,eV$, a conventional Slater integral scaling of 0.8 [22], a Lorentzian convolution of width 0.2 eV appropriate for the natural lifetime of the multiplet line (for a discussion of widths in $L_{2,3}$ edges see Ref. [23]), and a Gaussian convolution of width $\Delta E_0 = 0.3\,eV$, which will be justified in Section 4.1. A background contribution of the conventional form AE^{-r} has been added [24]. The spectrum is difficult to visualize in Fig. 2b, but the Fe 2p fine structure is clearly evident in the profile of this 2D image, obtained by integrating the signal along the non-dispersive y-axis (see lower part of Fig. 2).

The PSF presented in Fig. 2a is an experimental measurement of the ZL peak in the vacuum obtained by using a high dispersion (0.05 eV per channel). Inspection of the profile of the ZL peak (lower part of Fig. 2), reveals an energy resolution of about 0.9 eV at half maximum.

Fig. 2c shows the 2D image obtained on the detector by convoluting the model Fe $L_{2,3}$ edge with the experimental ZL peak and addition of Poisson noise. Figs. 2d–f show the reconstruction

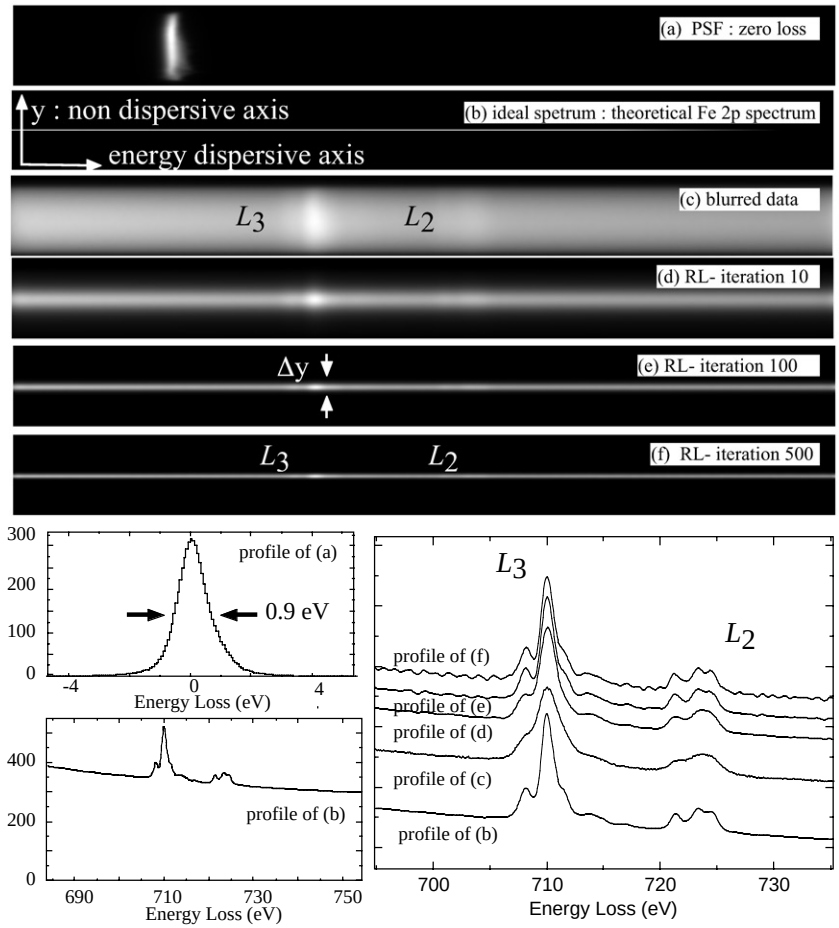

Fig. 2. Testing the RL deconvolution scheme on a simulated core edge: In the upper part, (a) PSF image, (b) theoretical Fe 2p image chosen as the perfect image, (c) blurred image analogous to an EELS observation, (d) deconvolution result using RL after 10 iterations, (e) the same after 100 iterations, and (f) the same after 500 iterations. In the lower part, the profiles obtained for the various electron energy loss images are showed.

using the RL method after 10, 100 and 500 iterations. It is evident that the image becomes narrower along the non-dispersive axis with an increasing number of iterations. Fig. 3 plots the average width Δy of the spectra, as measured by the full width at 20% of the maximum height along the y-axis, as a function of the iteration number. At iteration 0 (before restoration starts), the spectrum has a width of around 80 pixels (the non-dipersive axis of the CCD is made of 100 pixels). After 100 iterations, the width has reduced to about 8–10 pixels.

The profiles of the reconstructed image are also presented in the lower-right part of Fig. 2. After 10 iterations (profile d), it is clear that the spectrum is not yet fully reconstructed. In particular, the pre-peak located at the lower energy of the L_3 line is hardly separated from the main line and still only appears as a shoulder. The white line L_2 is also still composed of two broad features. After 100 iterations, the reconstructed spectrum displays more details. The two white lines exhibit all the fine structure present in the original spectrum. After 500 iterations, the fine structure exhibits increased visibility but the whole spectrum is characterized by a strong wavy structure. This degraded signal arises from the noise amplification effect mentioned in the previous section.

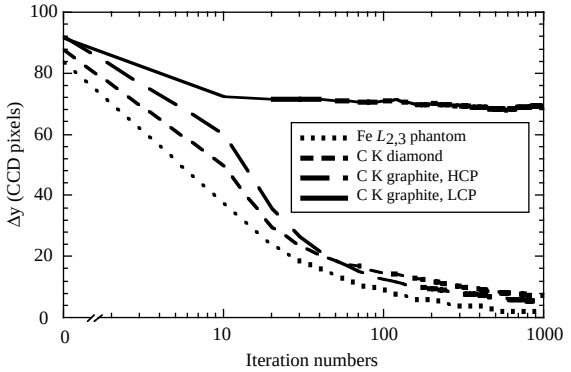

Fig. 3. Evolution of the width Δy measured by the full width at 20% of the maximum along the y-axis, as a function of iteration number. Such Δy can be seen in the EELS image of Fig. 2e and in the profile obtained along y-axis of Fig. 8e. The width for the Fe $L_{2,3}$ test image, the C-K diamond, the C-K graphite is measured using either an HCP or an LCP.

At this point, one might ask whether it is useful to restore spectra using a 2D approach since one is only interested in the intensities along the dispersion axis, i.e., a 1D domain. The answer to this question is not obvious. We have compared the efficiency of RL algorithm for restoring the Fe 2p phantom spectrum using four different approaches: (i) a 2D approach as presented in Fig. 2, (ii) a 2D approach using a Gaussian pre-filtering where the degraded image and the PSF are convoluted by a Gaussian of width $\sigma = 2$ pixels as suggested by van Kempen et al. [18], (iii) a 1D approach where we have used the profile of Figs. 2a and c as the PSF image and the starting image that is degraded, and (iv) a Gaussian pre-filtered 1D approach with $\sigma = 2$ pixels.

To evaluate the respective efficiency of these processes, we have calculated the signal-to-noise ratio of the reconstructed profile [12] as a function of the iteration number (k) defined as

$$S/N(k) = \sum_i \text{truth}_i \Big/ \sum_i |\text{truth}_i - \text{estimate}_i| = \sum_i O(i) \Big/ \sum_i \left|O(i) - O^{(k)}(i)\right|, \quad (2)$$

where the sums are computed over all pixels of the spectrum. For 2D reconstruction, the signal-to-noise ratios have been calculated for the 1D profile of the restored image. In fact, it is not meaningful to compare the 1D and 2D signal-to-noise ratios. The 2D S/N ratios are very poor although the reconstructed spectra appear quite good. Indeed, the ideal image consists of a one-pixel wide spectrum, whereas the reconstructed spectra still have non-negligible widths for iteration numbers as large as 500, which leads to low values for the S/N ratio. Furthermore, since one is only interested in an improvement in energy resolution, the meaningful true object is the 1D profile. The S/N should then be computed using this true object.

The S/N ratios, plotted in Fig. 4, exhibit all the same shapes that could be easily understood while looking at the image of residuals, i.e., perfect spectrum minus restored spectrum. The S/N ratios rapidly increase with the first iterations since the Fe 2p fine structure appears rapidly in the reconstructed spectra. At higher iteration numbers, the S/N is degraded due to the noise amplification effect. For intermediate values, the S/N exhibits a maximum. If we compare 1D and 2D restorations, the 1D restoration appears to be more efficient with an optimal restoration obtained at a higher iteration number. As expected, Gaussian pre-filtering in the RL algorithm gives better results [18]. In this case, pre-filtered applied to a 2D image yields a better reconstruction.

At that time, the difference between 2D and 1D RL method was not clear. On one hand, 1D restoration consumes less CPU time and exhibits a much faster convergence. On the other hand, the

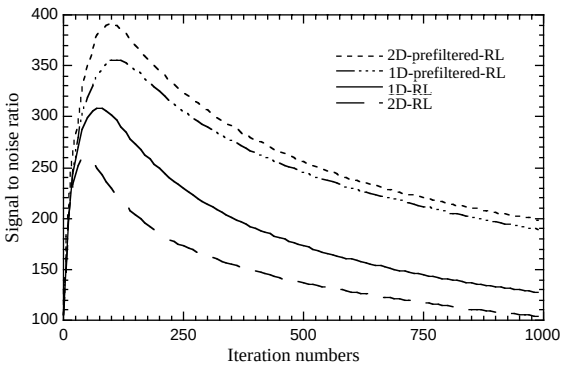

Fig. 4. Evolution of the S/N as a function of iteration numbers. Comparison of the 2D pre-filtered, 1D pre-filtered, 2D and 1D RL reconstruction process.

pre-filtered 2D RL method gives the best restoration results. The 2D *S/N* may be further improved if one only integrates the area of the CCD where the signal is the more intense to build the profile (see Section 3.1). It will also be shown that a 2D reconstruction may be advantageous to track restoration artifacts and helpful to evaluate an imperfect knowledge of the PSF.

3. Validity of the Richardson–Lucy approach for EELS spectroscopy

3.1. Diamond C-K edge

In this section, the RL method has been applied to the restoration of diamond C-K edge experimental spectra. Fig. 5 shows one raw experimental EELS spectrum and a few restored spectra using the RL deconvolution method. An abundant literature exists for these edges, resulting from EELS as well as XAS. Previous XAS studies [25–32] indicate that the energy range for diamond can generally be divided into two regions characterized by their specific features, namely at around 289 eV is the C 1s core exciton and between 290 and 302 eV is a relatively broad band of σ^* states. A large dip in the absorption spectrum occurs at around 302 eV, which can be attributed to a second absolute gap in the diamond band structure. The energy resolution of these XAS experiments ranges between 300 meV to better than 150 meV.

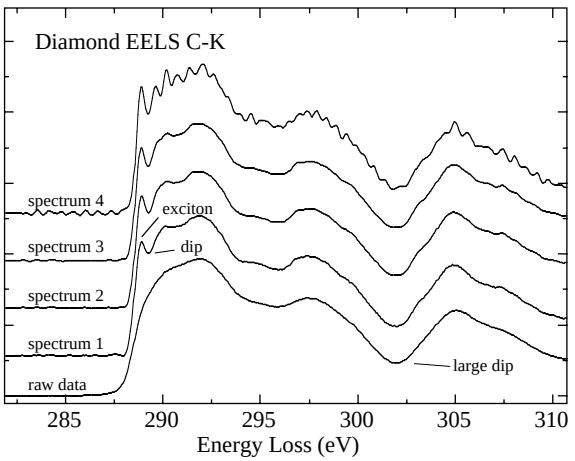

Fig. 5. Diamond EELS C-K spectra obtained after RL restoration. These spectra correspond to the four different restoration conditions arrowed in Fig. 7. The original raw data are also presented for comparison. Spectra are shown after background subtraction.

Several EELS experiments on the C-K diamond edge have been published [33–37] but only measurements performed using instruments fitted with a system capable of an energy resolution better than 300 meV exhibit all the expected fine structures [33–35]. The other EELS experiments [36,37] compare well with the non-restored raw data presented in Fig. 5.

Although all these high energy resolved studies exhibit the same features, the observed intensity can vary from one work to another. In particular, XAS experiments usually show more intense and sharper excitonic features. At least two reasons may explain this discrepancy. First, XAS experiments may have a better energy resolution. It has also been claimed by Batson and Bruley [34] that dynamic screening of the core exciton by the swift electrons involved in EELS experiment may influence the observed intensities as compared to the XAS experiments.

Chang et al. [30] have also observed that the C-K exciton line alters with the decrease of the diamond grain size due to the presence of a quantum confinement effect. According to the literature [31], the C-K exciton line may also be influenced by some disorder within the diamond structure, such as N impurities. Finally, Batson [33] shows that the exciton peak could be sensitive to EELS channeling. Although all these effects may not be important in our EELS scattering experiments, they are sufficient to preclude the idea of a perfectly known C-K reference. Nevertheless, the exciton line appears as a good test for RL deconvolution since only experiments achieved with an energy resolution better than 0.3 eV have resolved it.

Our experimental EELS spectrum has been recorded with a Topcon 002B TEM operated at 100 keV equipped with a LaB_6 gun and a modified Gatan PEELS model 666 EELS. The energy dispersion was set to 0.05 eV per channel. An under-heated filament was used to decrease the energy spread of the incident electron beam. In the

case of the C-K diamond edge, we used a focussed probe 30 nm in diameter with a convergence angle of $2\alpha = 30$ mrad and collection angle of $2\beta = 24$ mrad. Particular attention has been devoted to tilting the sample far from any strong diffraction conditions. A spectrum of the C-K edge has been collected by accumulating five spectra with a 2 s acquisition time per spectrum. With the same angular conditions, a ZL measurement has been acquired by accumulating approximately 100 spectra in the vacuum with 4 ms acquisition time per spectrum. These two spectra are gathered in Figs. 6a and b. This experimental setup has been determined by the following idea. Since the ZL measurement should be a good representation of the PSF of the core-loss spectrum, the illumination conditions at the entrance aperture of the spectrometer must be as close as possible for the two measurements. This is achieved using a collection angle smaller than the convergence angle. These two angles, both chosen to be much larger that the inelastic characteristic scattering angle $\theta_E = 1.5$ mrad for C-K edge, limit the influence of the inelastic scattering distribution on the core-loss spectrum. One also has to keep in mind that the diffraction pattern must not exhibit strong Bragg reflection. A restored spectrum obtained after 40 iterations is shown in Fig. 6c. Most of the intensity has been redistributed to within the central part of the CCD. In Fig. 3, the width Δy of the restored spectra is plotted as a function of the iteration number. Starting with a 90-pixel wide spectrum, after 100 iterations the width has shrunk to around 12–14 pixels. This result validates the selected angular setup. Indeed, the restoration seems to converge towards the expected perfectly double focussed spectrum. Compared to the test case of iron 2p edge, the convergence is slower. This may arise from a residual influence of the inelastic angular distribution, a slight defocus of the spectrometer during the 290 eV shift, or difference in the magnetic stray fields instabilities for the two measurements. Indeed, all these effects can lead to a degraded measurement of the PSF producing a poorer and slower restoration.

Let us now consider more precisely profiles obtained along the energy dispersive axis after RL restoration, such as the one shown in Fig. 6d. Spectra have been restored using several different processes including 1D restoration, 2D restoration, pre-filtered 2D restoration, centered 2D restoration (where the profile is obtained by integrating the 2D images for a limited width Δy centered at the maximum intensity), and centered and pre-filtered 2D restoration. To evaluate the respective efficiency of the different restoration methods, two parameters have been calculated and compared for each profile. The first parameter, which can be regarded as a fingerprint of the improvement in energy resolution, is determined from the intensity difference between the maximum

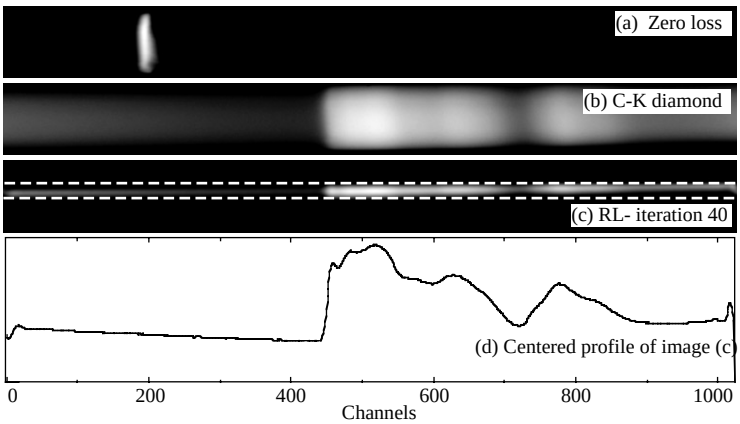

Fig. 6. CCD images measured for (a) a ZL in the vacuum, (b) a C-K edge for a diamond crystal, (c) restored images obtained after 40 RL iterations, and (d) profile obtained from the integration of the region constrained by the dashed lines in Fig. 6c.

of the exciton line and the dip adjacent to this exciton line. This intensity difference is calculated and normalized to the integrated number of counts within the first 20 eV of the edge, which is assumed to be constant and independent of the energy resolution. The resulting value appears to be sensitive to the visibility of the exciton line and is referred to as the "exciton line visibility". A second approach is to estimate the magnitude of the noise amplification. As mentioned before, the literature does not provide a C-K edge that can be regarded as an ideal spectrum, which prevents an easy calculation of the *S*/*N* ratio. We have therefore decided to calculate the *S*/*N* using Eq. (2) for the slow decreasing background located before the edge. The true signal has been estimated by fitting the background with a conventional inverse power law. This procedure gives good results, provided the *S*/*N* is calculated for a restricted energy range of 20 eV, where the inverse power law fit gives a good estimate of the true object. The evolution of the exciton line visibility with respect to the *S*/*N* ratio of the background is plotted in Fig. 7 for the different reconstruction procedures. It is evident that the 2D-restoration procedure is the least efficient. The 1D, pre-filtered 2D and centered 2D restoration show a significant enhancement compared to the basic 2D restoration. The more efficient restorations, as defined by an advantageous combination of the two parameters, are those obtained for a pre-filtered and centered 2D restoration. We have extracted four spectra at different positions shown by arrows in Fig. 7 and compared them with the original raw spectrum in Fig. 5. Spectrum 1 corresponds to an *S*/*N* ratio of 290, which can be compared with an *S*/*N* ratio of about 650 in the original spectrum. This spectrum has been obtained after 180 iterations of a 2D RL procedure. Spectrum 2 has the same *S*/*N* ratio but shows an improved restoration and has been obtained after 600 iterations for a pre-filtered and centered 2D RL procedure. Spectrum 3 is obtained with the same procedure but with an iteration number as high as 1000. Spectrum 4 is the result of 2000 iterations for a 1D RL procedure. It is evident that spectrum 2 is better resolved than spectrum 1 for an equivalent noise amplification. Spectrum 3 shows an even shaped exciton line but also worrisome noise amplification. For the last spectrum, the noise has become unacceptable and the exciton intensity might only be the result of the local conservation of the intensity combined with the noise amplification effect.

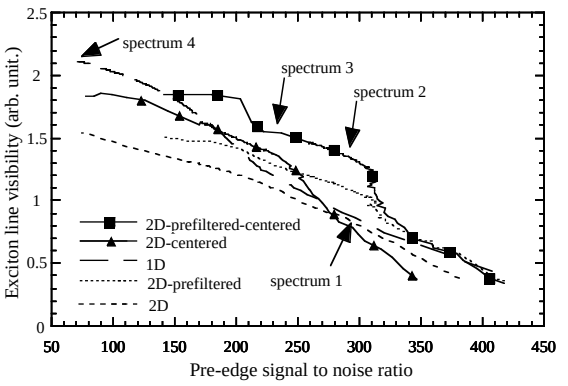

Fig. 7. Core exciton visibility as a function of the background *S*/*N*. The performance of the RL algorithm can be evaluated through an optimized combination of these two parameters. Comparison of the performance of 2D pre-filtered and centered, 2D pre-filtered, 2D centered, 2D and 1D RL reconstructions.

Three main results may be extracted from this C-K diamond study: (i) the measured ZL can be regarded as a good PSF for RL procedure; (ii) 2D restoration, with filtering and centering, gives the more promising results; (iii) the improvement in energy resolution is quite significant. Starting with an energy resolution of around 0.9 eV, comparison with previously published data allows us to assess a final energy resolution approaching 0.2 eV. In particular, spectrum 2 shown in Fig. 5, closely resembles the XAS measurement of Fayette et al. [27] using a high-energy monochromator.

3.2. Graphite C-K edge with a highly convergent probe (HCP)

In the two following sections, the restoration of the C-K edges for a graphite sample are described. Fine structure for this edge has been studied extensively by EELS and XAS over the past two decades [38–43]. In fact, studies dealing with "graphitic-like" C-K edges have known a large development as a consequence of the discovery of

fullerene molecules and nanotubulite compounds [44,45].

These previous studies have shown that the graphite 1s spectrum consists of a strong pre-peak at 285.5 eV with a π^* character (π orbitals are directed perpendicular to the basal plane of graphite) followed by a broad σ^* band (σ orbitals lie within the plane). The best energy resolved experiments also show a very sharp excitonic feature at around 291 eV. By using tunable, polarized synchrotron light, it is possible to excite a final state of a specific symmetry (σ^* or π^* band) from the 1s initial states. A strong variability of the σ^* and π^* peaks intensities can then be observed depending on the angle between the Pointing vector of the XAS radiation and the basal plane direction [39]. A similar symmetry dependence has been observed in EELS experiments depending on the choice of the convergence angle, the collection angle and the crystallographic direction of the crystal with respect to the incident electron beam [44,46].

In our experiments, the convergence and collection angles are chosen to be the same as for the diamond measurement. The direction perpendicular to the basal plane is set a few degrees off the optical axis. In this way, the diffracted intensities, which cannot be completely cancelled for such a crystalline compound so close to a major axis zone, are limited while keeping the π^* orbitals almost parallel to the optical axis.

Fig. 8a shows the ZL measurement in the vacuum. It is evident that the ZL peak has an 'S' shape. This is due to a stronger aberrated spectrometer working condition compared to the one used for the diamond measurements (characterized by the ZL peak in Fig. 6). The flattest aberration figure is not systematically searched since the RL deconvolution algorithm can correct it. Furthermore, by calculating the profile of this 2D image, an energy resolution (FWHM) of around 1.1 eV is measured, which can be regarded as a routine energy resolution for a LaB_6 TEM.

The 2D image of the graphite C-K is also shown Fig. 8b. One can easily see the two majors features (π^* and σ^* states) of this edge appearing as two broad peaks. The π^* distribution has also a strong 'S' shape. After 50 iterations using a pre-filtered

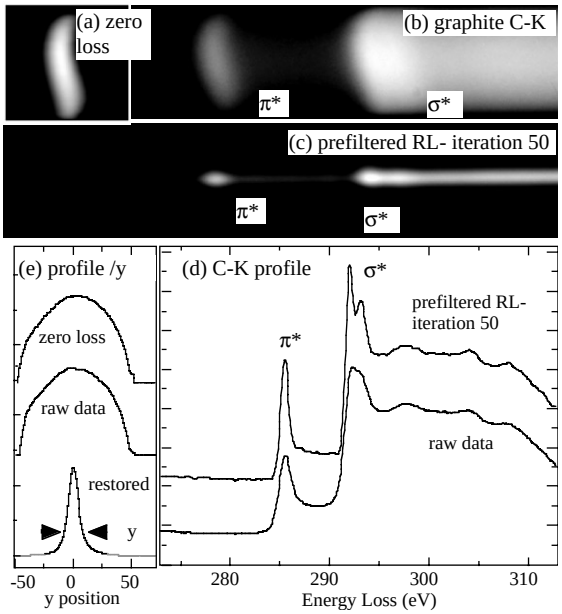

Fig. 8. Graphite C-K restoration. CCD images measured for (a) a ZL in the vacuum, (b) a C-K edge for a graphite crystal, (c) restored images obtained after 40 RL iterations, (d) profiles of image (b) and (c) demonstrating the improvement in energy resolution. In addition, the background has been removed, and (e) profile obtained along the y-axis for the ZL, the raw C-K measurement and the one obtained after 50 RL iterations. The width Δy shows a strong reduction during the restoration.

RL algorithm, the spectrum has strongly narrowed (see Fig. 8c). In particular, the π^* peak has become a small flattened spot. Here again, the measured width of the spectrum with respect to the iteration number is presented in Fig. 3 and shows a fast convergence towards a perfect double focussed spectrum. This is also strong evidence that the measured PSF is a well-behaved function in the RL algorithm. It is also informative to look at the intensity distribution along the y-axis, rather than along the energy dispersive axis, for these 2D images. The profiles obtained from the ZL image and the one from the C-K raw data (in fact we measure the profile at the position of the π^* peak) compare well as shown in Fig. 8e. This indicates that the inelastic angular distribution does not dominate the angular distribution of the 300 eV loss electrons. This angular blurring is likely to be a key point in obtaining a good PSF shape and

hence a good restoration. Indeed, it ensures that the PSF, $P(i-j)$, does not depend on the input data, $O(j)$. Otherwise, a deconvolution algorithm such as RL procedure would give poor result. One also notes that after restoration the profile shows a sharp symmetrical figure.

Fig. 8d displays the C-K profiles along the dispersive axis obtained before and after restoration. The sharp exciton line becomes unambiguously visible after RL processing. Despite noise amplification, the broad features in the fine structure at higher energy loss are still identifiable. Comparing this spectrum with the previously published data, we can confidently argue that the final energy resolution of the EELS system is better than 300 meV.

3.3. Graphite C-K edge with a low-convergent probe (LCP)

The previous angular choice enables a quick and highly efficient RL restoration. Nevertheless, it requires a convergence angle at least equal to the collection angle. In this section, we investigate the possibilities of restoring spectra using a quite opposite experimental setup compared to the previous one, i.e., with a LCP ($2\alpha = 2$ mrad) and a much larger collection angle ($2\beta = 38$ mrad). In addition, as flat as possible an aberration figure has been achieved. Crystallographic orientation of the graphite sample was the same as in Section 3.2, i.e., the basal plane was almost perpendicular to the optical axis.

Fig. 9 first displays the ZL measurement in the vacuum. The image obtained has a reduced spatial expansion along the non-dispersive axis. This arises from the low-angle distribution of the incident electron beam. The measured C-K exhibits much wider features. In particular, the σ^* intensities almost cover the whole y-axis. The difference between the two traces (1 and 2) at different y positions reveal a strong symmetry selection along the y-axis. Indeed, the π^* peak has a stronger intensity for trace 1. Looking at Fig. 9, the ZL measurement may not be regarded as a perfect PSF function for the core loss. Since the ZL measurement has only a narrow angular distribution, most of the optical paths of the

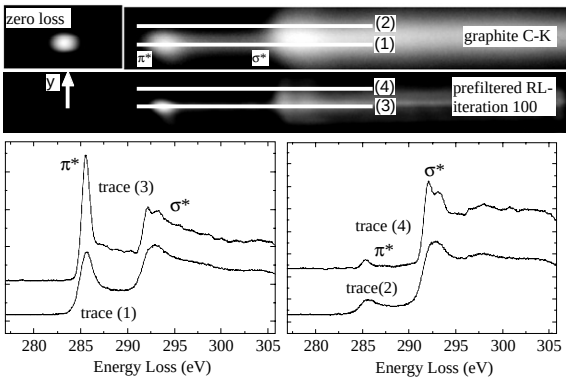

Fig. 9. In the upper part, CCD images measured for a ZL in the vacuum, a C-K edge for a graphite crystal and the restored images obtained after 100 RL iterations. In the lower part, traces obtained at various y positions in the previous images. For the traces, the backgrounds have been removed according to an inverse power law.

spectrometer are not represented in the PSF. However, the robustness of RL algorithm towards PSF error and the choice of a flat aberration figure, may lead to a successful mixed energy resolution/angular dependency restoration. The image obtained after 100 iterations is also displayed in Fig. 9. At first sight, the π^* contribution has strongly been reduced along the y-axis whereas the σ^* distribution still covers a large section of the y-axis. The average width Δy of the spectrum as a function of the iteration number shows a weak reduction, demonstrating that a strong part of the angular distribution is not taken into account by the PSF. The spectrum is not converging towards a double focussed spectrum. Examination of traces 3 and 4, obtained at the same positions as in the raw data, shows that the exciton line has become visible and that the anisotropy effects have been enhanced. As expected, the final energy resolution appears poorer than for the experiment shown in Section 3.2. In addition, noise has been strongly amplified.

The ratios between the peak π^* maximum and the exciton line maximum (σ^*) as a function of the trace position y, have been calculated and the results for the raw data, and the restored images (at 10 and 50 iterations) are plotted in Fig. 10. One can easily see that the symmetry selection is strongly enhanced by the RL process. For the

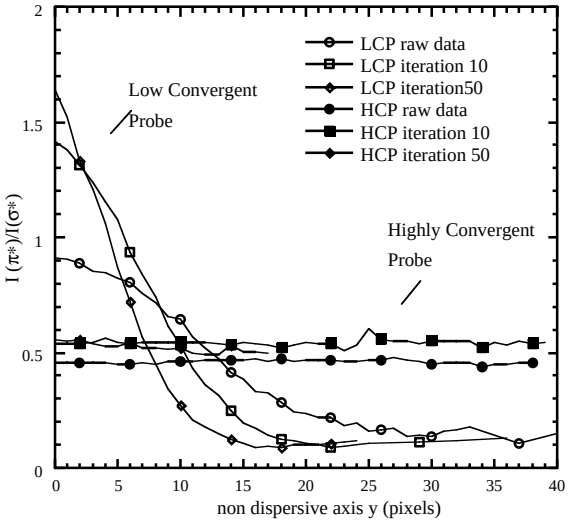

Fig. 10. : Evolution of the $I(\pi^*)/I(\sigma^*)$ ratio with the y-trace position for the raw image and various restored image (after 10 and 50 iterations). Results obtained from EELS measurements acquired with HCP (Section 3.2) and with LCP (Section 3.3) are compared.

$y = 0$ position, the restored spectra (after 50 iterations) show a much more intense π^* contribution compared to the raw data. Indeed, $I(\pi^*)/I(\sigma^*)$ ratio increases from a value of about 0.9 to about 1.6. At position $y = 10$ pixels, the restored spectra exhibit reduced π^* intensities. This crossover of the ratio demonstrates that the RL algorithm is also efficient at pointing out the symmetry selection rules. If a ratio change occurred due to energy resolution improvement, no crossover would be observed. Fig. 10 also displays these ratios calculated for the graphite experiments realized with a higher convergence angle (see Fig. 8 and Section 3.2). In this case, the ratio does not change with the y position. This is also a good indication that the angular dependency from the sample scattering is blurred. A slight difference in the $I(\pi^*)/I(\sigma^*)$ ratio is observed between the unrestored and restored spectra that could be easily explained by the strong energy resolution improvement.

Two conclusions may be driven from these sets of restoration. First, the RL process is robust enough to be used for a large range of angle distributions. Of course, the final energy resolution would not show the same benefit depending on the correctness of the PSF function. Second, the RL may help to amplify symmetry selection in EELS experiments.

4. Application to iron-based oxides

In this section, the RL algorithm has been applied to the restoration of the Fe 2p and O 1s spectra in reference samples of hematite Fe_2O_3, magnetite Fe_3O_4 and siderite $FeCO_3$ of mineralogical origin [47]. Indeed these edges are known to exhibit very sharp features rarely revealed in EELS experiments. Furthermore, the restoration of these edges may be regarded as more challenging compared to the previous C-K edge reconstruction, since they imply higher energy losses and lower elemental concentrations. In particular, we believe that the spectrometer defocus for high-energy loss could be a strong limitation of the RL restoration. Several options may be used to limit these defocussing effects. First, a weak chromatic aberration coefficient C_c of the objective lens is an important advantage: the ultra-high-resolution pole piece of the Topcon TEM, with a C_c of 0.8 mm used for this work, is highly favorable. Longer camera lengths, which provide a smaller spectrometer source in the focal plane of the projector lens, can also be recommended. If necessary, one can measure the PSF in vacuum with a reduced energy beam corresponding to the energy loss of interest. Then, the high voltage may be raised for the core-loss collection.

To optimize the restoration, the same angular conditions as described in Section 3.1 have been chosen. Then, 2D RL restorations have been conducted, the iteration process being stopped after 50–100 iterations, depending on the magnitude of the noise amplification. In these EELS experiments, the energy resolution prior to the restoration is around 1.2 eV because of a slightly under-heated LaB_6 filament.

4.1. Fe $L_{2,3}$ edges

EELS spectroscopic studies of the $L_{2,3}$ white lines for transition metals (TM) have always been

a topic of primary interest. Indeed, the comparison with the abundant XAS works on these edges indicates that EELS may provide a unique tool to investigate at a nanometer scale the valencies, the charge transfer, the spin state and even some magnetic ordering of the TM bearing materials [46, 48–50]. Unfortunately, most of the EELS studies provide a limited amount of information because of an insufficient energy resolution. Indeed, the natural lifetime broadening of the multiplet lines involved in the TM 2p spectra are about a few tenths of an eV and the typical values of the various orbital splitting may not exceed a few eV. Thus, the regular EELS energy resolution of around 1 eV introduces a noticeable blurring of the features of the TM $L_{2,3}$ edges.

The restored edges shown in the bottom of Fig. 11 exhibit several well-resolved features of fine structure, compared to that observed in the raw data, also reproduced at the top of Fig. 11. In particular, hematite and siderite compounds display about 10 different features over the 15 eV of the peak extent. In fact, these edges can be well described within a nearly atomic description involving excitations from the $2p^6 3d^n$ Fe ground state towards the $2p^5 3d^{n+1}$ states, where $n = 5$ for Fe^{3+} and $n = 6$ for Fe^{2+} [23,51]. The theoretical Fe^{3+} spectrum chosen as the phantom spectrum of Section 2, satisfactorily reproduces the experimental hematite spectrum. Since the theoretical spectrum includes convolution with a Gaussian of 0.3 eV width, the final energy resolution of the

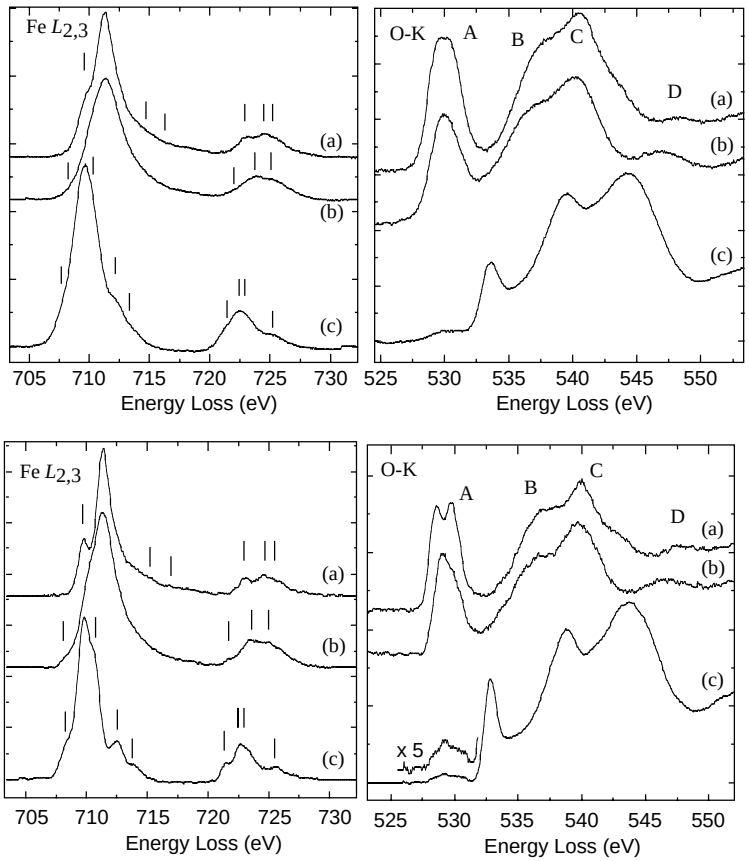

Fig. 11. Iron 2p and O 1s spectra for reference minerals: (a) hematite, (b) magnetite, (c) siderite after RL restoration. Raw data are also presented in the upper part of the figure and exhibit very few of the sharp features in the fine structure. Spectra are displayed after background subtraction. For the Fe $L_{2,3}$ spectra, the important features of the fine structures have been marked with short vertical lines.

EELS system after deconvolution can then be reasonably estimated to have this value.

For a more detailed description of all the features appearing on both sides of the $L_{2,3}$ white lines, one can refer to the paper of Kuiper et al. [52] for Fe^{3+} compounds and for the Fe^{2+} bearing materials to the well documented paper of Cheng et al. [53]. All the features of the fine structure marked in Fig. 11 can be identified in these previous XAS experiments, which further confirms the reliability of the RL algorithm.

For the magnetite spectrum, the L_3 line shows no strong features in agreement with previous published work [54,55]. This absence of noticeable features has several intrinsic origins. First, magnetite is a metal, displaying a non-zero density of states with Fe 3d character at the Fermi level [56]. The electronic behaviors of the iron Fe 3d states are then poorly described within a nearly atomic description. In addition, the existence of a site multiplicity and a mixed valence tends to increase the spectroscopic blurring [55]. Here again, the result of the RL iterations provides a spectrum with no artifactual features.

4.2. O-K edges

Oxygen K-edges for these samples are also shown in Fig. 11 prior to and after the RL procedure. The hematite and magnetite spectra display four main features labeled (A, B, C, and D), the origin of which has already been discussed in previous studies [57,58]. In particular, the first region (labeled A) exhibits prominent features after RL restoration. For hematite, there are two visible components separated by 1.2 eV, whereas for Fe_3O_4 one of the components only appears as a shoulder at 0.7 eV to the high-energy side of the other. These shapes are in good agreement with those observed with XAS [54,57]. As an example, one can look at the spectrum obtained recently by Kendelewicz et al. [54] using a Standford Synchrotron Radiation Line equipped with a spherical grating monochromator, for which the energy resolution is not specified but seems to be comfortably below 0.3 eV. To our knowledge, previous high-energy resolved XAS or EELS O-K edges for siderite have not been reported. However, the present EELS measurements exhibit several sharp peaks as well as a feeble pre-edge feature that may arise from a weak hybridization between the O 2p and the Fe 3d orbitals.

5. Conclusion

In conclusion, the use of RL algorithm has been shown to be of great benefit in the field of EELS. Indeed, it significantly improves the energy resolution of our EELS spectra. The following significant results have obtained:

(i) *Different convergence and collection angles:* A reasonable restoration of the graphite C-K edge has been demonstrated using either a low convergence or a HCP. The method is particularly efficient if one uses the following angular prescription: $\alpha \geqslant \beta; \alpha, \beta \gg \theta_E$ and weak diffraction conditions. Under these conditions, the measured ZL can be regarded as a good PSF for the core loss and the RL algorithm rapidly converges towards a perfectly double focussed spectrum. The final energy resolution is then only limited by noise amplification, energy instabilities of the spectrometer and accelerating voltage, and spectrometer defocus. Comparison with previous EELS and XAS experiments, indicates that it is possible to reach a final energy resolution of around 0.2–0.3 eV, even when the measurements have been performed with a LaB_6 thermionic source providing an initial energy spread of around one electron volt.

(ii) *Application to a large number of edges* (C-K, O-K, Fe $L_{2,3}$) *and materials* (*diamond, graphite, Fe bearing minerals*): In addition to the data that has been presented, the RL procedure has been used to restore Mn and Ni edges in oxide materials and has given valuable additional information relative to the EELS raw data. In particular, the application of the RL restoration for studying the thermal decomposition of the siderite sample, for which there is an alteration of Mn and Fe valencies with temperature, will be soon published [47].

(iii) *Various restoration strategies.* We have obtained a favorable result using 1D, 2D, or pre-filtered RL algorithm. As mentioned in Section 3.1, the use of 2D restoration with Gaussian pre-filtering and selection of the higher S/N pixels to rebuild the profile, gives the best results. In addition, one can track restoration artifacts looking at the 2D reconstruction and how the spectrum converges or does not converge towards a double focussed spectrum. For all these approaches, the restored spectra fit well with the expected spectra and RL restoration can be regarded with confidence. This is not surprising since RL procedure is already known to give highly quantifiable image restoration in other scientific fields due to its capabilities for local and global intensity conservation.

For all these reasons, we are convinced that RL restoration is a promising technique in the EELS domain, and can be considered in many cases as a valuable alternative to the implementation of monochromators on the primary beam of electrons. In addition, we are currently working on restoration methods that can correct for some of the difficulties with the conventional RL method, in particular, instabilities due to energy drift and noise amplification.

Acknowledgements

We wish to thank A. Isambert for providing the siderite sample, and D. Imhoff for stimulating discussions.

References

[1] M. Terauchi, et al., Microsc. Microanal. Microstruct. 2 (1991) 351.
[2] K. Tsuno, J. Rouse, J. Electron Microsc. 45 (1996) 417.
[3] M. Troyon, Microelectron. Eng. 6 (1987) 105.
[4] H.W. Mook, P. Kruit, Ultramicroscopy 81 (2000) 129.
[5] H. Rose, Ultramicroscopy 56 (1995) 11.
[6] M.H.F. Overwijk, D. Reefman, Micron 31 (2000) 325.
[7] W.H. Richardson, J. Opt. Soc. Am. 62 (1972) 55.
[8] L.B. Lucy, Astrophys. J. 79 (1974) 745.
[9] J.M. Zhuo, Microsc. Res. Tech. 49 (2000) 245.
[10] EELS spectra database, http://www.cemes.fr/~eelsdb/ and XAS publications database, http://scon155.phys.msu.su/~papers/.
[11] J.L. Starck, F. Murtagh, Publ. Astron. Soc. Pacific 110 (1998) 193.
[12] J. Nunez, J. Llacer, Publ. Astron. Soc. Pacific 108 (1993) 1192; A.F. Boden, D.C. Redding, R.J. Hanisch, J. Mo, J. Opt. Soc. Am. A 13 (1996) 1537; I.C. Busko, in: R.J. Hanish, R.L. White (Eds.), The Restoration of HST Image and Spectra II, Space Telescope Institute, Baltimore, 1994, p. 279.
[13] D.L. Snyder, C.W. Helstrom, A.D. Lanterman, M. Faisal, R.L. White, in: R.J. Hanish, R.L. White (Eds.), The Restoration of HST Image and Spectra II, Space Telescope Institute, Baltimore, 1994, p. 139.
[14] T.J. Cornwell, Proceedings of the NATO Advanced Study Institute on Diffraction-Limited Imaging with Very Large Telescope, Cargèse, 1998, p. 273.
[15] K. Nakashima, H. Takami, Proceddings of ESO/OSA Topical Meeting on Astronomy with Adaptive Optics Present Results and Future Programs European Southern Observatory, Garching bei München, Germany, 7–11 September 1998.
[16] L.A. Shepp, Y. Vardi, IEEE Trans. Med. Imag. MI-1 (1982) 113.
[17] K.M. Perry, S.J. Reeves, in: R.J. Hanish, R.L. White (Eds.), The Restoration of HST Image and Spectra II, Space Telescope Institute, Baltimore, 1994, p. 97.
[18] G.M.P. van Kempen, L.J. van Vliet, P.J. Verveer, H.T.M. van der Voort, J. Microsc. 185 (1997) 354.
[19] R.L. White, In: R.J. Hanish, R.L. White (Eds.), The restoration of HST Image and Spectra II, Space Telescope Institute, Baltimore, 1994, p. 104.
[20] R. Molina, J. Mateos, J. Abad, In: R.J. Hanish, R.L. White (Eds.), The Restoration of HST Image and Spectra II, Space Telescope Institute, Baltimore, 1994, p. 118.
[21] F.M.F. de Groot, J.C. Fuggle, B.T. Thole, G.A. Sawatzky, Phys. Rev. B 42 (1990) 5459.
[22] A. Gloter, V. Serin, Ch. Turquat, C. Cesari, Ch. Leroux, G. Nihoul, Eur. Phys. J. B 22 (2001) 179.
[23] F.M.F. de Groot, J.C. Fuggle, B.T. Thole, G.A. Sawatzky, Phys. Rev. B 41 (1990) 928.
[24] R.F. Egerton, Electron Energy Loss Spectroscopy in the Electron Microscope, 2nd Edition, Plenum Press, New York London, 1996.
[25] M.M. Garcia, I. Jimenez, L. Vasquez, C. Gomez-Ameixandre, J.M. Albella, L.J. Terminello, F.J. Himpsel, Appl. Phys. Lett. 72 (1998) 2105.
[26] M. Lübbe, P.R. Bressler, D. Drews, W. Braun, D.R.T. Zahn, Diamond Rel. Mater. 7 (1998) 247.
[27] L. Fayette, B. Marcus, M. Mermoux, G. Tourillon, K. Laffon, P. Parent, F. Le Normand, Phys. Rev. B 57 (1998) 14123.
[28] Y. Ma, N. Wassdahl, P. Skytt, J. Guo, J. Nordgren, P.D. Nordgren, J.E. Rubennson, T. Boske, W. Eberhardt, S.D. Kevan, Phys. Rev. Lett. 69 (1992) 2598.

[29] Y. Ma, P. Skytt, N. Wassdahl, P. Glans, D.C. Mancini, J. Guo, J. Nordgren, Phys. Rev. Lett. 71 (1993) 3725.
[30] Y.K. Chang, H.H.H. Hsieh, W.F. Pong, M.H. Tsai, F.Z. Chien, P.K. Tseng, L.C. Chen, T.Y. Wang, K.H. Chen, D.M. Bhusari, J.R. Yang, S.T. Lin, Phys. Rev. Lett. 82 (1999) 5377.
[31] G.J. Flynn, L.P. Keller, H. Hill, C. Jacobsen, S. Wirick, Lunar Planet. Sci. XXXI (2001) 1904.
[32] D.M. Gruen, A.R. Krauss, C.D. Zuiker, R. Csencsits, L.J. Terminello, J.A. Carlisle, I. Jimenez, D.G.J. Sutherland, D.K. Shuh, W. Tong, F.J. Himpsel, Appl. Phys. Lett. 68 (1996) 1640.
[33] P.E. Batson, Phys. Rev. Lett. 70 (1993) 1822.
[34] P.E. Batson, J. Bruley, Phys. Rev. Lett. 67 (1991) 350.
[35] H. Hirai, M. Terauchi, M. Tanaka, K. Kondo, Diamond Rel. Mater. 8 (1999) 1703.
[36] T.J. Bernatowicz, P.C. Gibbson, R.S. Lewis, Astrophys. J. 359 (1990) 246.
[37] V. Serin, E. Beche, R. Berjoan, O. Abidate, D. Rats, J. Fontaine, L. Vandenbulcke, C. Germain, A. Catherinot, in: J.L. Davidson, W.D. Brown, A. Gicquel, B.V. Spytsin, J.C. Angus (Eds.), Proceedings of the Fifth International Symposium on Diamond Materials, The Electrochemical Society, Pennington, NJ, 1998, p. 126.
[38] P.E. Batson, Phys. Rev. B 48 (1993) 2608.
[39] R.A. Rosenbergen, P.J. Love, V. Rehn, Phys. Rev. B 33 (1986) 4034.
[40] I. Jimenez, D.G.J. Sutherland, T. Van Buuren, J.A. Carlisle, L.J. Terminello, F.J. Himpsel, Phys. Rev. B 57 (1998) 13267k.
[41] E.L. Shirley, Phys. Rev. Lett. 80 (1998) 794.
[42] A.J. Papworth, C.J. Kiely, A.P. Burden, S.R.P. Silva, G.A.J. Amaratunga, Phys. Rev. B 62 (2000) 13628.
[43] R.D. Leapman, P.L. Fejes, J. Silcox, Phys. Rev. B 28 (1983) 2361.
[44] O. Stéphan, E. Sandré, P.M. Ajayan, F. Cyrot-Lackman, C. Colliex, Phys. Rev. B 53 (1996) 13824.
[45] K. Suenaga, E. Sandré, C. Colliex, C.J. Pickard, H. Kataura, S. Iijima, Phys. Rev. B 63 (2001) 165408.
[46] N.K. Menon, J. Yuan, Ultramicroscopy 74 (1998) 83.
[47] A. Isambert, A. Gloter, J.P. Valet, F. Guyot, J. Geophys. Res., to be published.
[48] A. Gloter, J. Ingrin, D. Bouchet, C. Colliex, Phys. Rev. B 61 (2000) 2587.
[49] L.A.J. Garvie, P.R. Buseck, Nature 396 (1998) 667.
[50] P.A. van Aken, B. Liebscher, V.JS tyrsa, Phys. Chem. Min. 25 (1998) 323.
[51] G. van der Laan, I.W. Kirkman, J. Phys. Cond. Matter 4 (1992) 4189.
[52] P. Kuiper, B.G. Searle, P. Rudolf, L.H. Tjeng, C.T. Chen, Phys. Rev. Lett. 70 (1993) 1549.
[53] G. Peng, J. van Elp, H. Jang, L. Que, W.H. Armstrong, S.P. Cramer, J. Am. Chem. Soc. 117 (1995) 2515.
[54] T. Kendelewicz, P. Liu, C.S. Doyle, G.E. Brown Jr., Surf. Sci. 469 (2000) 144.
[55] J.P. Crocombette, M. Pollack, F. Jolet, N. Thromat, M. Gautier-Soyer, Phys. Rev. B 52 (1995) 3143.
[56] Z. Zhang, S. Satpathy, Phys. Rev. B 44 (1991) 13319.
[57] Z.Y. Wu, S. Gotta, F. Jollet, M. Pollak, M. Gautier-Soyer, C.R. Natoli, Phys. Rev. B 55 (1997) 2570.
[58] H. Kurata, E. Lefevre, C. Colliex, R. Brydson, Phys. Rev. B 56 (1993) 13763.